Advantages of Structure and Electrochemical Properties of Graphene Prepared from Tectonically Deformed Coal

Hang Zhang, Yugui Zhang,* Jian Li, and Zhangnan Ma

Read Online

ACCESS | Metrics & More | Article Recommendations

ABSTRACT: Asa low-cost carbon-rich resource, coal has been widely used to prepare excellent electrochemical energy-storage carbon materials such as graphene. However, the different structures of carbon source will affect the performance of carbon materials. To explore the feasibility of preparing high-performance graphene from the carbon source affected by tectonic stress in coal, in this paper, series products of coal-based graphene are prepared by tectonically deformed coal (TDC) and normal structural coal (NSC). The structural parameters are characterized by HRTEM, XRD, Raman, and low-temperature CO_2 and N_2 adsorption, and the electrochemical performance of coal-based graphene lithium battery is tested by galvanostatic charge−discharge and cyclic voltammetry. The results show that tectonic stress makes the proportion of the medium-long aromatic fringes, preferred orientation degree (POD), and multilayer stacking in TDC aromatic fringes slightly higher than those in NSC. At the same temperature, the relatively large microcrystalline size, the high order degree, and more pore structures make the local molecular oriented (LMO) domain vertical height (d) and graphitization degree (G) of the coal-based graphite microcrystalline structure prepared by TDC better than those of NSC, which indicates that the carbon source in TDC contains more graphitizable carbon structures. This makes the graphene prepared by TDC not only possess perfectly ordered crystal planes but also relatively abundant nanochannels. High lithium-storage capacity and low charge-transfer resistance make the electrochemical performance of graphene prepared by TDC as an anode electrode material for lithium-ion batteries superior to that by NSC.
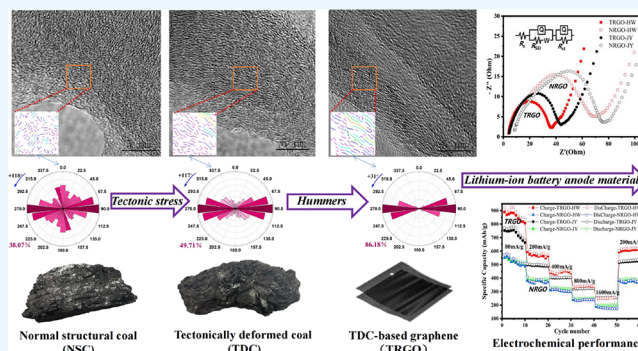
1. INTRODUCTION

With the acceleration of global energy consumption, graphite and graphene have become strategic resources.[1,2] Rosalind Franklin produced seminal papers on the graphitizable structure of carbon source earlier.[3,4] Utilizing XRD analysis, she divided the graphitizing carbons formed by carbon sources with different structures at 1000−3000 °C into two different and clearly defined categories, graphitizable carbon and nongraphitizable carbon, and summarized two necessary conditions to make given carbon sources easy to graphitize. First, the cross-linking system that combines the neighboring crystallites in the material should not be too strong; second, it is also a more basic condition that neighboring crystallites should have a strong tendency to lie in a nearly parallel orientation. In the nongraphitizing carbons, crystallite growth is impeded both by the strong cross-linking between neighboring crystallites and by their random orientation. Therefore, it is particularly important to explore carbon sources with a graphitizable carbon structure to prepare graphite and graphene.

The industrial formation of graphite requires heating of appropriate carbon source precursors to nearly 2800 °C in an inert atmosphere.[5] However, in the natural context, some carbon source precursors in metamorphic rocks are transformed into graphite at a temperature ∼ close to 450−500 °C.[6] The temperature required to form natural graphite is low, and as a consequence, it is generally considered that natural graphitization is controlled mainly by temperature with additional influences of pressure, duration of the metamorphic event, and shear strain.[7−12] In the material sciences field, the study of graphitization of synthetic carbon precursors heat-treated under pressure has shown that some carbon source precursors, which are not graphitizing under the effect of temperature at ambient pressure, could graphitize by adding hydrostatic or oriented pressures.[13−15] Thus, adding additional
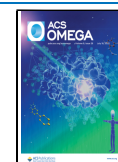
factors like pressure may contribute to producing better carbon source precursors, thereby reducing energy consumption.

Coal is a low-cost carbon-rich resource, and coal-based graphite and coal-based graphene have received increasing attention in recent years because of the natural similarity between aromatic carbon structures and carbon material structures.[16,17] In the past, researchers have successfully designed and constructed coal-based carbon nanomaterials with rich structure and morphology according to the characteristics of carbon sources in coal with different metamorphic degrees.[18−22] However, there are few studies on the influence of pressure on the characteristics of carbon sources in coal, and the directional pressure is an important factor for the formation of graphitized carbon source precursors. Tectonically deformed coal (TDC) is the product of coal seam compression and shearing by geological structure, and its crystalline structure perhaps records the tectonic features.[23,24] Almost all coal and gas outburst accidents are related to TDC, and thus, the study of TDC has attracted extensive attention.[25,26] With the help of coal structure testing technologies, the research group has compared and studied the microcrystalline structure characteristics and small molecular structure evolution of TDC and normal structural coal (NSC) and concluded that under the action of tectonic stress, the coal molecular structure is activated and then polymerizes and decomposes. On the one hand, when the tectonic stress acts on the basic structural unit of the aromatic ring of coal, the molecular structure is oriented during growth, and a larger aromatization macromolecular structure is formed by polymerization.[24] On the other hand, the side chains and functional groups on the aromatic ring structure of TDC will decompose to form low-molecular-weight compounds and discharge gaseous hydrocarbons (gas), which weakens the originally strong cross-linking system in the coal structure.[27,28] The results of polymerization and decomposition reactions of coal structures caused by tectonic stress are similar to the two necessary conditions for the graphitizable carbon set by Rosalind Franklin, which guides the direction for the preparation of graphite and graphene from TDC.

As an electrode material, graphene has a broad application prospect in lithium-ion batteries (LIBs).[29] Raw material cost and core technology breakthroughs are the two bottlenecks restricting the scale development of the graphene industry.[30,31] The key to solving this problem is to seek cheap and high-quality original materials and efficient conversion technology. The structural evolution of coal is significantly affected by tectonic geological factors, and the difference in carbon source will eventually affect the structure and performance of graphene products. However, currently, research on the preparation of graphene and its derivatives using coal as a carbon source is still in its infancy. Therefore, research on the influence of the original structure and material composition of coal under tectonic geological action on graphene products based on coal should be strengthened. In view of the general trend of world energy development toward green, low carbon, and efficient utilization, as well as the abundant resources and inherent microcrystalline structure properties of TDC, this study selects two groups of TDC/NSC samples to prepare coal-based graphene series products. High-resolution transmission electron microscopy (HRTEM), X-ray diffraction (XRD), Raman, and low-temperature CO_2 and N_2 adsorption techniques were used to characterize the differences in microcrystalline and pore structure parameters of coal-based

graphene series products. Using constant current charge discharge and cyclic voltammetry (CV), the electrochemical performance of LIBs carrying graphene series products was investigated. The objective is to reveal the feasibility to prepare high-performance graphite and graphene from TDC and explore a new direction for the high value-added utilization of TDC resources and the low-carbon preparation of coal-based graphite and coal-based graphene.

2. SAMPLES AND EXPERIMENTS

2.1. Coal Sample Selection and Pretreatment. Two TDC/NSC groups of contrast anthracites from Hongwei (HW) mine, Hunan Province, China, and Jiyuan (JY) mine, Henan Province, China, are selected as the raw materials. As shown in Figure 1a,c, the surface of TDC-HW and TDC-JY
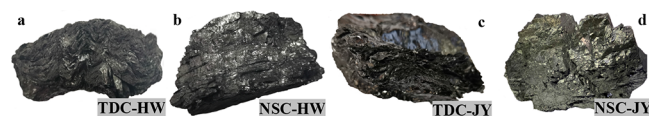

Figure 1. Macro coal sample characteristics of TDCs/NSCs.

samples significantly affected by tectonic stress has obvious folds, the bedding structure completely disappears, the cross section is broken, and the coal is very soft and easily pinched into a scaly powder. According to the classification scheme of TDCs by Ju and Wang,[32,33] it can be determined that TDC-HW and TDC-JY are mylonitic coals most affected by tectonic deformation. However, the surface of NSC-HW/JY, which is collected from the same coal seam and not damaged by tectonic stress, has clear bedding and a stepped uneven fracture with vitrinite characteristics on the cross section (Figure 1b,d), and the coal is extremely hard. Each coal sample is crushed, ground, and screened to 74 μm or below and is taken for later use.

To avoid the influence of minerals in coal on the structure quantitative analysis and graphitization process of subsequent samples, the coal samples are demineralized in advance according to the method of Nyathi et al.[34] After demineralization, anthracite samples are marked as T-HW, N-HW, T-JY, and N-JY. The basic sample characteristics are shown in Table 1.

2.2. Sample Preparation. *2.2.1. Preparation of Coal-Based Graphite.* According to the method of Rodrigues et al.,[17] all demineralized anthracites were placed in the carbonizer and carbonized at 1000 °C for 1 h under vacuum conditions, and then the carbonized samples were placed in the graphitization furnace and kept at 2800 °C for 2 h to obtain graphite samples (collectively referred to as G; the TDC-based graphite is referred to as TG, and the NSC-based graphite is referred to as NG). The product samples are named as TG-HW, NG-HW, TG-JY, and NG-JY.

2.2.2. Preparation of Coal-Based Graphene by Thermal Reduction. According to the method of Huan et al.,[18] the coal-based graphite samples were oxidized by the modified Hummers method,[35,36] and the corresponding graphene oxide (GO) samples were obtained by exfoliation. The resulting coal-based graphene oxides were labeled TGO-HW, NGO-HW, TGO-JY, and NGO-JY, respectively.

GO samples were placed into a muffle furnace for heat treatment at 900 °C for 5 min, and the cooled product was subjected to heat treatment at 900 °C for 5 min again. The

Table 1. Basic Characteristics of the Anthractie Samples Used[a]

coal sample number	structure type of coal body	$R_{o,max}$/%	proximate analysis (ωt %)			ultimate analysis (ωt %, daf)				
			M_{ad}	A_d	V_{daf}	C	H	N	S	O*
T-HW	TDC	4.00	3.27	0.33	6.52	93.37	2.64	0.62	0.69	2.68
N-HW	NSC	3.57	3.81	0.61	8.11	91.36	2.04	0.85	0.89	4.86
T-JY	TDC	5.60	3.37	0.25	4.25	93.17	2.57	0.55	0.59	3.12
N-JY	NSC	5.44	3.43	0.24	4.46	92.31	2.13	0.76	0.57	4.23

[a]Note: $R_{o,max}$, maximum reflectance of vitrinite in oil immersion; M, moisture; ad, air-dry basis; A, ash yield; d, dry basis; V, volatile matter; daf, dry ash-free; ωt %, weight percent.

obtained product was soaked in ethanol, sonicated for 3 h, and dried at 60 °C in a blast drying oven to obtain each coal-based graphene sample (collectively referred to as RGO). The sample numbers are TRGO-HW, NRGO-HW, TRGO-JY, and NRGO-JY.

2.3. Sample Testing and Characterization.

2.3.1. HRTEM. HRTEM uses a TECNAI G2 F20 field emission transmission electron microscope from the American FEI company, with an acceleration voltage of 200 kV, a point resolution of 0.24 nm, and a line resolution of 0.102 nm. After the sample passes through the 200 mesh sieve, ethanol is added and the sample is treated with ultrasonic vibration for 10−30 min. Then, two to three drops of the sample are collected and dropped onto a microgrid, and the sample is observed.

Quantitative image analysis (Reindeer Graphics software) in Adobe Photoshop was used to obtain aromatic fringes following the methods of Mathews et al.[37] The digital extraction of aromatic fringes is shown in Figure 2. First, the
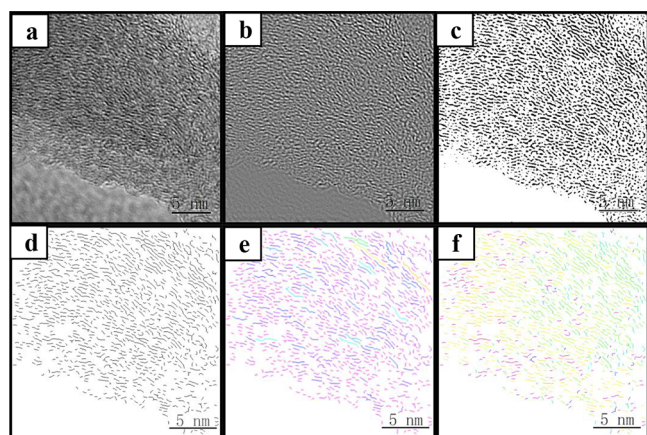

Figure 2. Digitalization process of aromatic fringes. Taking sample T-HW as an example, (a) original HRTEM micrograph, (b) micrograph after FFT and IFFT, (c) binary micrograph, (d) skeletonized micrograph, (e) false-colored micrograph by length, and (f) false-colored micrograph by angle.

image boundaries and segmented fringes at the boundary were removed to form a square (512 pixels × 512 pixels) micrograph (Figure 2a). Following grayscale selection and histogram shaping manipulations, an ideal fast Fourier transform filter was employed within a semiautomated sequence (Figure 2b). Using threshold function selection and skeleton information extraction, corresponding binary images were obtained (Figure 2c). Unrealistic fringes with large curvatures and noises, as well as fringes less than 3 Å, were removed to obtain a vectorized micrograph (Figure 2d). Length, angle, and relative position of aromatic fringes were obtained. Aromatic fringes were marked according to the

length or angle in certain bins, and corresponding digitally false-colored micrographs (Figure 2e,f) were obtained. Based on the Graphical User Interface constructed by Louw, the stacking of aromatic fringes was extracted.[38] Finally, several areas nearly parallel in alignment were selected, using Digital Micrograph software to measure the spacing between adjacent aromatic fringes and the vertical stacking height of the local molecular-oriented (LMO) domain.

2.3.2. XRD. The crystal structure of each sample was characterized by XRD using Cu-Kα radiation (λ = 0.15406 nm), a scanning range of 5−80°, and a scanning speed of 10°/min. According to the calculation method given in ref 39, the interlayer spacing (d_{002}), the crystallite height (L_c), the crystallite width (L_a), the average number of aromatic layers (N_{ave}), and the graphitization degree (G) were calculated.

2.3.3. Raman Spectroscopy. The Invia Reflex laser confocal micro-Raman spectroscopy system (Renishaw, UK) was used to test the molecular structure of the samples. The laser wavelength was 532 nm, and the wavenumber range was 500−3000 cm^{-1}. Each spectrum was subjected to peak fitting with Origin software to resolve the curve using a Gaussian curve-fitting module. The obtained parameters include the peak position (frequency, cm^{-1}), full width at half-maximum (FWHM, cm^{-1}), and I_{D1}/I_G.[40]

2.3.4. Pore Structure. Two gas injection methods, low-temperature CO_2 (with the Quadrasorb SI pore analyzer, saturation temperature at 273 K and relative pressure of 0.05−0.99) and N_2 adsorption (with the Autosorb-iQ-MP pore analyzer, saturation temperature at 77 K and relative pressure of 0.001−0.995) are used in this paper to jointly characterize the micropores (0−2 nm) and mesopores (2−36 nm) of the material. According to the single-layer adsorption theory test principle[41] and the pore classification scheme of IUPAC,[42] the low activation and diffusion rate of N_2 cannot accurately characterize the nanopores less than 2 nm. However, the molecule diameter of CO_2 gas is smaller, the saturation pressure of CO_2 at the saturation temperature (273 K) is higher, the diffusion rate is faster, and thus it can test 0−2 nm micropores.[43] In addition, the traditional BET and BJH models have a large error in the analysis of materials containing micropores, and the underestimated pore size can reach more than 20%.[44] To ensure the correlation and consistency of the data, the authors suggest using the DFT model, whose accuracy has been recommended by ISO and IUPAC organizations to characterize the micropore and mesopore of materials, and accumulating the pore data of each coal (1.5−2 nm) and RGO (1−2 nm) samples in the low-temperature N_2 adsorption test in the corresponding blank date that is not detected by low-temperature CO_2, so as to minimize the data error of experimental caused by the test principle and calculation model.
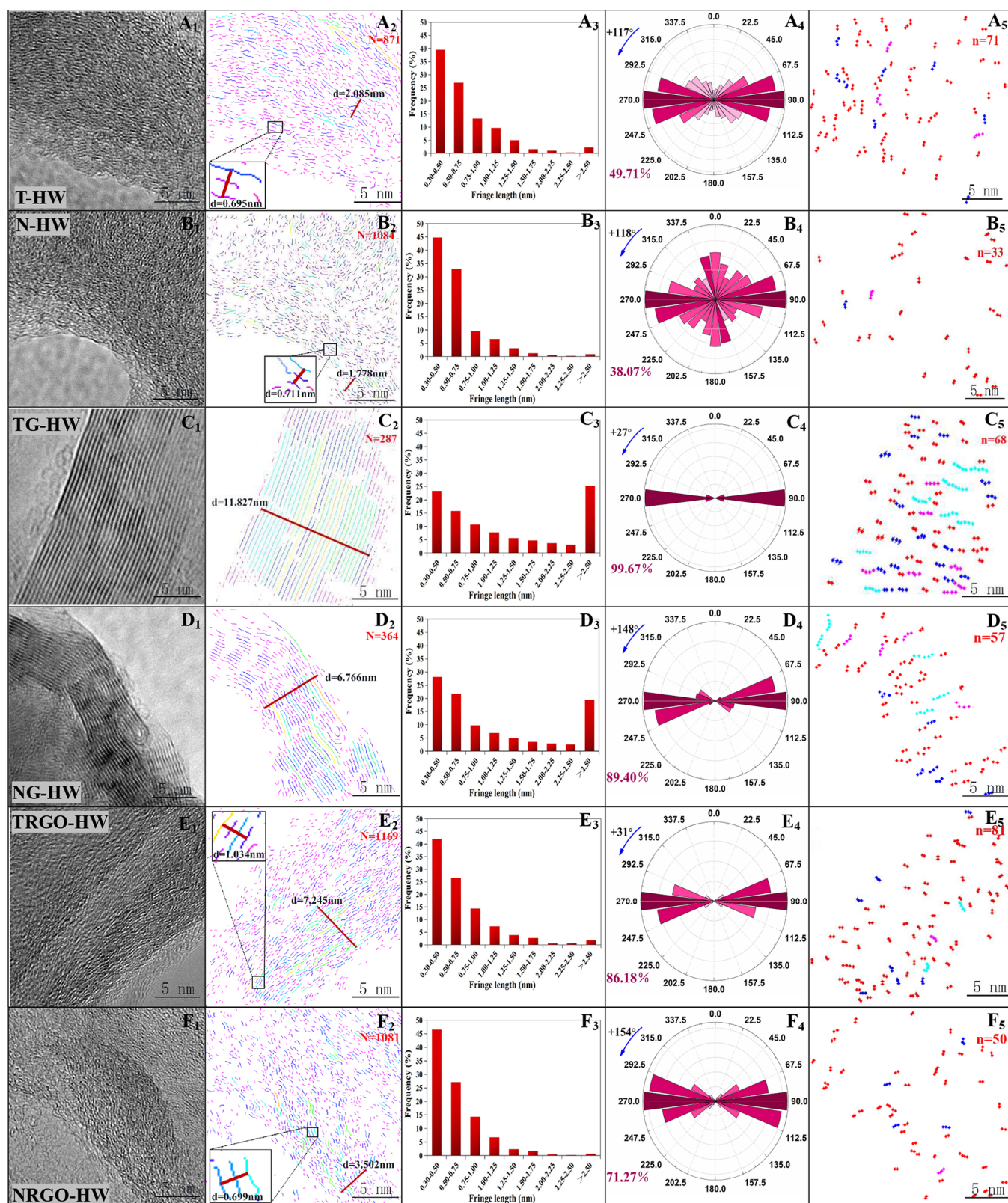
Figure 3. Distribution characteristics of aromatic fringes of anthracite, graphite, and graphene series samples. Taking Hongwei series samples as an example, (A_1-F_1) original HRTEM micrographs, (A_2-F_2) false-color micrographs by length, (A_3-F_3) fringe length distribution corresponding histogram, (A_4-F_4) rose directional diagrams, and (A_5-F_5) stacking distribution diagrams.

2.3.5. Electrochemical Performance Test of Coal-Based Graphene. The prepared RGO, polyvinylidene fluoride, and acetylene carbon black were fully mixed in the ratio of 8:1:1, and an appropriate amount of *N*-methyl pyrrolidone was added

to make a slurry that was later coated on the copper foil. After drying, the electrode sheet with a diameter of 12 mm was pressed. A lithium sheet was selected as the reference electrode, a polypropylene membrane was used as the

Table 2. Comparison of Characteristic Parameters of Aromatic Fringes of Anthracite, Graphite, and Graphene Series Samples

sample numbers	0.3–0.75 nm short fringes (%)	0.75–2.25 nm medium fringes (%)	>2.25 nm long fringes (%)	POD (%)	individual fringes (%)	2 stacks (%)	3 stacks (%)	>4 stacks (%)
T-HW	66.55	31.13	2.32	49.71	90.24	6.89	1.84	1.03
N-HW	77.69	21.39	0.92	38.07	96.68	2.86	0.18	0.28
TG-HW	39.14	35.58	25.28	99.67	66.50	12.32	7.88	13.30
NG-HW	49.91	30.66	19.43	89.40	76.10	11.26	3.57	9.07
TRGO-HW	68.52	29.65	1.83	86.18	91.79	6.07	1.20	0.94
NRGO-HW	73.72	25.63	0.65	71.27	94.82	4.16	0.74	0.28

diaphragm, and 1 mol/L $LiPF_6$ was dissolved in a solvent of vinyl carbonate and dimethyl carbonate with a volume ratio of 1:1 as the electrolyte. In a glovebox filled with argon, the components were assembled into a button battery (CR2032) for electrochemical performance evaluation. A battery test system (BT2013A, Lanbo, CHN) was used for the galvanostatic charge–discharge (GCD), rate performance, and cycle stability tests (voltage range: 0.01–3 V). An electrochemical workstation (CHI660, Chenhua, CHN) was used to obtain the CV curve (voltage range: 0.01–2.5 V, scanning speed: 0.2 mV/s) and AC impedance spectrum (100 kHz–0.01 Hz).

3. RESULTS AND DISCUSSION

3.1. HRTEM Analysis. In order to explore whether the coal, whose carbon source is affected by tectonic stress, has the aromatic structure advantage of preparing graphite and graphene, in this study, the aromatic fringe morphological distribution characteristics of carbon source structures in the process of synthesizing graphene from coal with different coal body structures were analyzed and tracked by HRTEM. Taking Hongwei series samples (T/N, TG/NG, and TRGO/NRGO) as an example (Figure 3), the morphological characteristics of aromatic fringes involve the occurrence of a single aromatic fringe and its combination, including length, orientation, and stacking.[45–47]

3.1.1. Morphology and Spacing Aromatic Fringes of Raw Materials and Process Products. In anthracite raw materials (Figure 3A₁,B₁,A₂,B₂), the aromatic fringes of T/N-HW show a distribution of random orientation and the basic structure units (BSUs) formed by adjacent aromatic fringes with short in-plane transverse extension, and the common vertical stacking height (d) is 0.695–2.085/0.711–1.778 nm. The BSUs are stacked and interrupted by amorphous regions represented by heteroatoms, functional groups, and bridging-bonds,[48] and micropores and stacking dislocations between adjacent BSUs are generally visible. The average spacing between nearly parallel in alignment adjacent aromatic fringes of T/N-HW is approximately 0.3475/0.3555 nm.

In graphite products (Figure 3C₁–D₁,C₂–D₂), the aromatic fringes are basically linear, and there are only small defects in the plane. The transverse extension length and vertical stacking height of BSU are significantly increased, and more BSUs form a highly ordered larger LMO domain, and the LMO domain stacking height of TG/NG-HW is approximately 11.827/6.766 nm. The average spacing between adjacent aromatic fringes of TG/NG-HW is 0.3359/0.3368 nm, which is within the range of natural crystalline graphite value (0.3354–0.3370 nm).[49]

In addition, in graphene products (Figure 3E₁–F₁,E₂–F₂), although the micropores and stacking dislocations between adjacent BSUs are denser than those of coal samples, the BSUs of graphene have a significant directional arrangement trend

compared with coal samples. The LMO domain stacking heights of TRGO/NRGO-HW are 7.245/3.502 nm. The value of average spacing between adjacent aromatic fringes of TRGO/NRGO-HW increases to 0.3450/0.3495 nm compared with those of the graphite products, which is smaller than those of the anthracite raw materials.

3.1.2. Aromatic Fringes Growth Advantage of TDC as a Carbon Source. As shown in Figure 3A₂–F₂, approximately 287–1169 aromatic fringes are used to determine the length distribution in these micrographs. The ductility of aromatic fringes of all samples at lengths of 0.30–2.50 nm shows a similar distribution, which decreases exponentially with the increasing fringe length (Figure 3A₃–F₃). The authors call the aromatic fringes within the range of 0.30–0.75 nm as short fringes, 0.75–2.50 nm as medium fringes, and those larger than 2.50 nm as long fringes. Table 2 shows that the proportion of medium and long fringes of T-HW is slightly higher than that of N-HW, while the proportion of short fringes decreases, which confirms that strong tectonic stress has an obvious transformation effect on the aromatic fringes of coal, indicating that tectonic stress has become the driving force for the growth of the coal aromatic structure, and the stress polycondensation mechanism will increase the size of polycyclic aromatic rings in coal.[46] Combined with the $R_{o,max}$ values of TDCs being greater than those of NSCs (Table 1), it reflects that the tectonic stress has promoted the advanced evolution of coal organic structure.[24,27,50] After high-temperature graphitization, the morphology of aromatic fringes of coal has significantly changed. The short aromatic fringes of coal-based graphite rapidly disappear, while the proportion of long fringes significantly increases, indicating that the essence of graphitization of coal lies in the splicing of aromatic fringes of coal.[51] Among them, the proportion of medium and long fringes of TG-HW is 35.58/25.28%, slightly higher than that of NG-HW, which is 30.66/19.43%. This result indicates that TDC has better aromatic fringe ductility advantage than NSC, and it is easier to obtain efficient splicing and extension at the same high temperature. After exfoliation, the proportion of medium and long fringes of TRGO-HW was significantly higher than that of NRGO-HW, which indicates that the excellent "growth" advantage of TDC is more conducive to the preparation of graphene products with large aromatic lamellae.

3.1.3. Aromatic Fringes Orientation Advantage of TDC as a Carbon Source. A significant advantage of HRTEM is that it can directly observe the directivity of aromatic fringes. Using the methods of Mathews and his collaborators Song et al.,[37,46] the structural order of aromatic fringes in coal-based graphene series samples can be characterized by the angular distribution of fringes. Theoretically, if the orientation of aromatic fringes is a random distribution, the proportion of total fringes should be 25% in the continuous 45° range. Any distribution higher or lower than this value shows a dominant distribution of

aromatic fringes; the higher the value, the better the orientation of aromatic fringes in the sample. According to this suggestion, after the whole micrograph is rotated (Figure 3A$_4$–F$_4$), the proportion of aromatic fringes within the range of 67.5°–112.5° is defined as the preferred orientation degree (POD), and the orientation of aromatic fringes is characterized by the strength of the POD index. Almost all directions of the rose diagram can be seen in N-HW (Figure 3B$_4$); therefore, the dispersion of aromatic fringes is large, and the POD is only 38.07%, while the POD of T-HW associated with it is 49.71% (Figure 3A$_4$), indicating that the order of aromatic fringe structure in TDC is higher. Based on the characteristics of the graphitizable carbon structure that neighboring crystallites should have a strong tendency to lie in nearly parallel orientation[4] and the POD value of TG-HW (99.67%) is higher than that of NG-HW (83.40%), it is believed that tectonic stress will increase the graphitizable carbon structure of carbon source in coal. Compared with NRGO-HW products, whose POD is 71.27%, TRGO-HW products inherit the excellent order of TDC-based graphite, and their POD is as high as 86.18%. The excellent "orientation" advantage of TDC makes it easier to prepare highly ordered graphene products than NSC.

3.1.4. Aromatic Fringes Stacking Advantage of TDC as a Carbon Source. The stacking of aromatic fringes can reflect the orientation and continuity of adjacent aromatic fringes.[37,38,51] Figure 3A$_2$–F$_2$ shows that the stacking style of aromatic fringes of various carbon materials is mainly face-to-face and stepped, and the adjacent aromatic fringes in stacking tend to be in parallel alignment. Figure 3A$_5$–F$_5$ shows a simplified stacking distribution diagram. There are many individual fringes without stacking in the T/N-HW coal samples (Table 2). Although the POD value of T-HW is higher than that of N-HW, due to the small extension length of the corresponding aromatic fringes of T-HW, the proportion of multistacking in T-HW is only slightly higher than that of N-HW, which indicates that the transformation of lattice fringes by tectonic stress is short-range order. After high-temperature graphitization of coal, the proportion of multistacking of TG/NG-HW rapidly increases to 33.50/23.90%. This occurs because adjacent BUSs, which were originally blocked by heteroatoms, functional groups, and bridging bonds used to form microporous structures, have grown and linked under the action of high temperature by lateral extension and vertical stacking, causing the rupturing of pore walls and flattening of adjacent BSUs, which results in the formation of a new highly polymerized LMO domain from the originally dispersed BSUs. Among them, the layered stacking ratio of TG-HW is significantly higher than that of NG-HW (Table 2), indicating that the short-range ordered microcrystalline orientation growth state of TDC makes it contain more graphitizable carbon structures, which makes TDC under high temperature easily produce LMO domain with longer fringes, a higher POD value, and a better stacking effect. Finally, the highly ordered TG-HW provides the material basis for oxidation-intercalation of graphene, which makes the prepared TRGO-HW "inherit" the stacking advantage of its precursor TG-HW, resulting in the stacking ratio of the TDC-based graphene (8.21%) and the vertical height of LMO domain (7.245 nm) better than those of the NSC-based graphene (5.18% and 3.502 nm). This result shows that the excellent "stacking" advantage of TDC makes it easier to produce graphene products with a more ordered and perfect crystal plane than the NCS.

3.2. XRD Analysis.
The XRD patterns of various carbon materials at each stage are similar (Figure 4a–d), but the peak
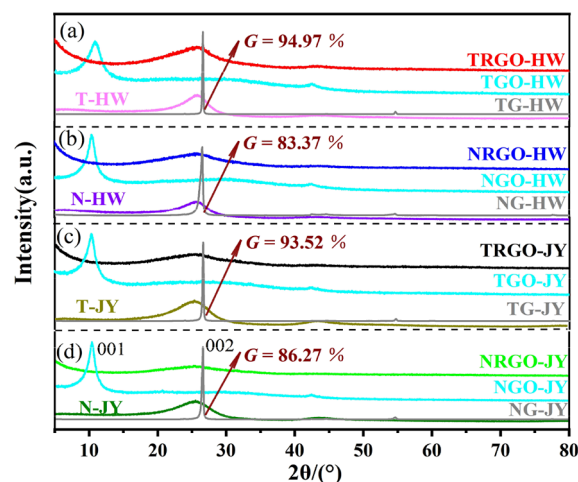

Figure 4. XRD patterns of anthracite, graphite, GO, and RGO series samples.

shapes of the anthracite, graphite (G), GO, and graphene (RGO) series samples from different precursors are significantly different. The (002) peak of the anthracites show a high background intensity, indicating that there is a large amount of amorphous carbon structure in the anthracites.[51] In combination with Table 3, it is found that d_{002} of TDC is smaller than that of NCS, and the grain size (L_a, L_c) is larger, which is consistent with the result that the aromatic fringes of TDC described by HRTEM are relatively long and the spacing between adjacent fringes is short. It is confirmed that the tectonic stress will lead to the microcrystalline orientation growth of the coal organic structure. After graphitization at 2800 °C, the (002) peak of each graphite product becomes extremely sharp, and the d_{002} value of each graphite is smaller than the natural graphite (0.3371 nm) value, indicating that the graphitization degree (G) of the prepared graphite products is better than that of natural graphite (80.23%).[17] Among them, the graphitization degree (G) of TG is greater than that of NG, which reflects that TDC may contain more graphitizable carbon structures than NCS, resulting in the L_a, L_c, and N_{ave} of TG being significantly higher than those of NG. Then, after the oxidation of graphite, the graphite characteristic peak (002) practically disappears, and a relatively large graphite oxide characteristic peak (001) appears at approximately 10.92°, which shows that the strong oxidant effectively intercalates graphite, causing the expansion between graphite sheets. Finally, after thermal reduction and ultrasonic exfoliation, the strong (001) peak of GO disappeared, and the reduction of oxygen-containing functional groups led to the enhancement of interlayer van der Waals force, which prompted a wide and weak (002) peak near 25.52° for each RGO, indicating that the graphene lamellae of RGO are laminated and aggregated again, and the crystal plane tends to be perfect. Zhou et al. considered that the higher graphitization degree is of great benefit to the intercalation of graphite by the oxygen-containing groups during oxidation,[53] thereby exfoliating graphene better. The L_a, L_c, and N_{ave} of TRGO are higher than those of NRGO (Table 3), and the L_a of TRGO is higher than that of the microcrystalline structure of graphene prepared by Wangtaipu normal structural anthracite as

Table 3. XRD Structural Parameters of Anthracite, Graphite, and RGO Series Samples[a]

sample numbers	$2\theta_{002}$ (°)	$2\theta_{100}$ (°)	d_{002} (nm)	L_a (nm)	L_c (nm)	G (%)	N_{ave}
T-HW	25.72	42.90	0.3461	3.975	1.815	—	6.24
N-HW	25.42	43.48	0.3501	3.721	1.794	—	6.12
T-JY	25.58	43.06	0.3480	3.889	1.802	—	6.18
N-JY	25.44	43.42	0.3498	3.833	1.798	—	6.14
TG-HW	26.52	42.44	0.3358	54.451	38.868	94.97	116.75
NG-HW	26.44	42.38	0.3368	38.713	18.979	83.37	57.35
TG-JY	26.51	42.36	0.3360	48.388	31.393	93.52	94.43
NG-JY	26.46	42.44	0.3366	42.498	22.058	86.27	66.53
TRGO-HW	25.87	42.57	0.3441	7.115	1.158	—	4.37
NRGO-HW	25.45	43.97	0.3497	5.878	1.008	—	3.88
TRGO-JY	25.62	43.46	0.3474	6.777	1.128	—	4.25
NRGO-JY	25.52	43.87	0.3488	6.299	1.023	—	3.93

[a]Note: G, degree of graphitization; N_{ave}, average number of aromatic layers; —, not detected.
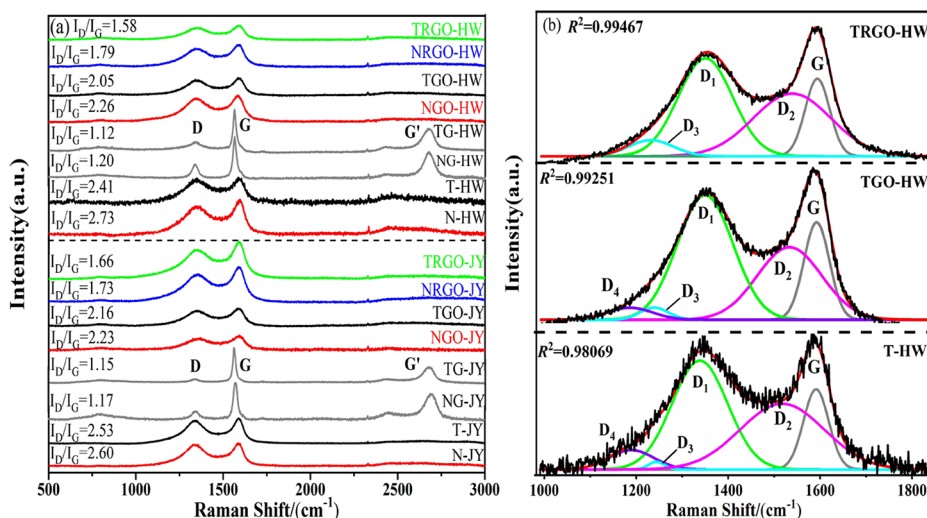

Figure 5. Raman patterns of anthracite, graphite, GO, and RGO series samples. (a) Original Raman spectral feature; (b) first-order modal peak fitting feature of Raman spectra.

described in the literature,[18] which indicates that it is easier to prepare graphene with a perfect crystal plane from TDC.

3.3. Raman Analysis. The Raman spectrum can provide information on defects and stacking of carbon material lamella.[54] As shown in Figure 5a, the analysis of the Raman spectrum mainly focuses on the in-plane vibration of graphite sp^2 carbon atoms (G peak, ~1580 cm^{-1}), graphite lattice defects and the edge disorder (D peak, ~1345 cm^{-1}), and the multistacking mode of carbon atoms (G′ peak, ~2700 cm^{-1}).[55] To more accurately analyze the defect structure changes in each phrase of RGO synthesized from anthracite, the D peak was fitted separately to obtain the D_1–D_4 peak bands (taking the T-HW series samples as an example, Figure 5b); for detailed attribution of spectral generation, please refer to refs 40, 56, in which the D_1 peak is usually referred to as the defect band, which is related to graphite lattice imbalance or defects introduced by heteroatoms, and the fitting curves have a good fitting degree ($R^2 > 0.98$). The half-peak width ratio (I_{D1}/I_G) and the peak position difference (G–D_1) of the D_1 and G peaks represent the graphitization degree and aromatic ring condensation degree of the sample, respectively. The smaller the I_{D1}/I_G or the larger the G–D_1, the better the order of carbon atoms reflected and vice versa. The structural parameters after peak fitting of each samples are summarized in Table 4.

Table 4. Structure Parameters of Samples by Raman Spectrum Fitting[a]

sample numbers	D_1/cm^{-1} frequency	D_1/cm^{-1} FWHM	G/cm^{-1} frequency	G/cm^{-1} FWHM	G–D_1/cm^{-1}	I_{D1}/I_G
T-HW	1338	135	1591	56	253	2.41
N-HW	1347	158	1593	59	246	2.68
T-JY	1339	114	1590	45	251	2.53
N-JY	1343	122	1592	47	249	2.60
TG-HW	1328	28	1584	25	256	1.12
NG-HW	1335	36	1586	30	251	1.20
TG-JY	1330	30	1584	26	254	1.15
NG-JY	1333	34	1585	29	252	1.17
TGO-HW	1346	127	1588	62	242	2.05
NGO-HW	1355	149	1590	66	235	2.26
TGO-JY	1348	138	1588	64	240	2.16
NGO-JY	1352	145	1589	65	237	2.23
TRGO-HW	1328	106	1588	67	260	1.58
NRGO-HW	1339	136	1590	76	251	1.79
TRGO-JY	1331	116	1588	70	257	1.66
NRGO-JY	1336	128	1589	74	253	1.73

[a]Note: FWHM, half-peak width; (G–D_1), peak position difference; (I_{D1}/I_G), half-peak width ratio.
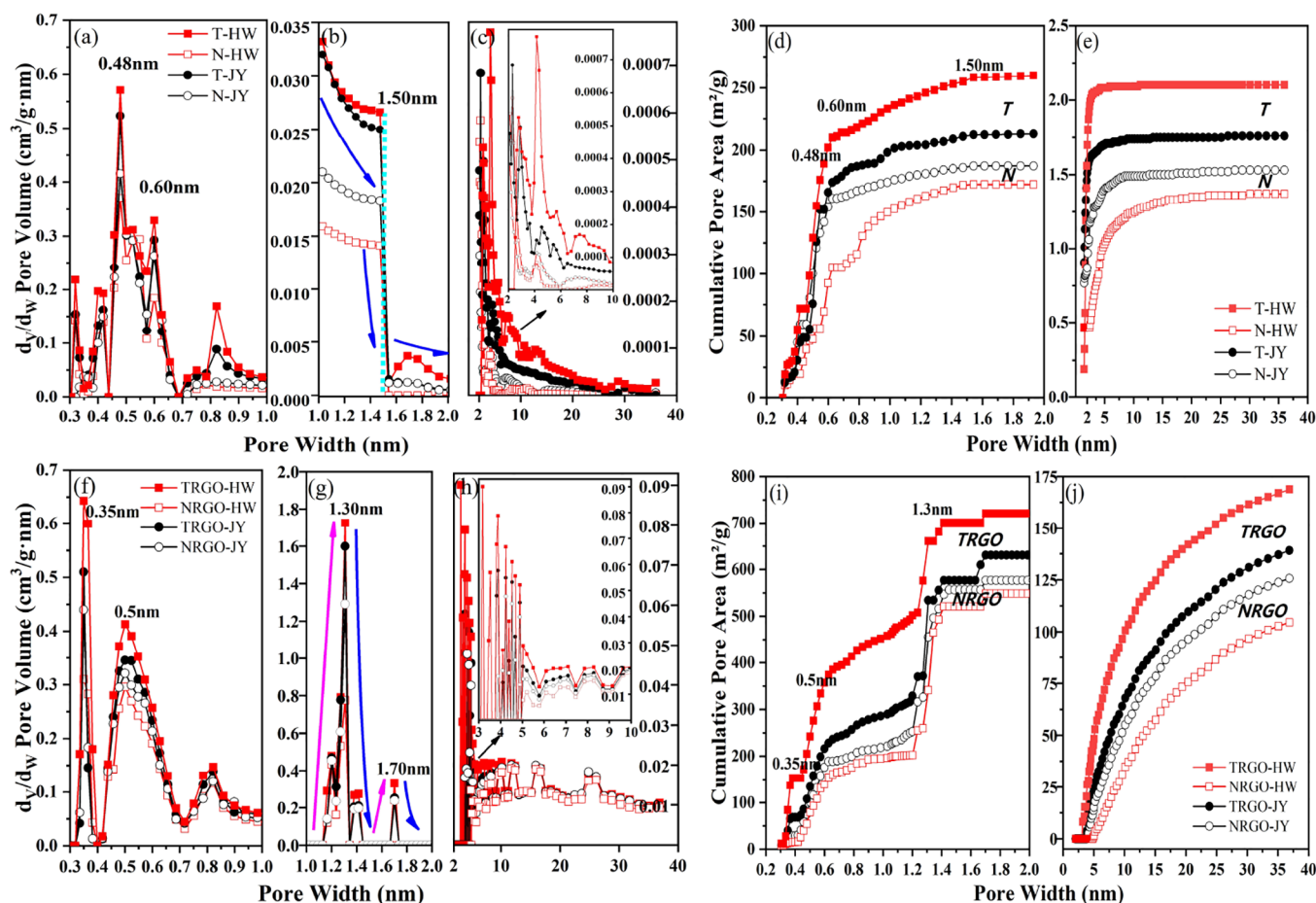
Figure 6. Distribution characteristics of the pore structure of anthracite and RGO series samples. (a−c) Pore size distribution of anthracite samples, (d−e) cumulative pore area of anthracite samples, (f−h) pore size distribution of RGO samples, and (i−j) cumulative pore area of RGO samples.

Table 5. Specific Pore Structure Parameters of Anthracite and RGO Series Samples[a]

sample numbers	V_{Total} (cm³·g⁻¹)		V_{Total} (%)		S_{Total} (m²·g⁻¹)		S_{Total} (%)	
	V_1	V_2	V_{x1}	V_{x2}	S_1	S_2	S_{x1}	S_{x2}
T-HW	0.0794	0.0028	96.59	3.41	259.9	2.1	99.20	0.80
N-HW	0.0578	0.0015	97.47	2.53	172.3	1.4	99.19	0.81
T-JY	0.0679	0.0020	97.13	2.87	212.9	1.8	99.16	0.84
N-JY	0.0607	0.0018	97.12	2.88	187.3	1.5	99.21	0.79
TRGO-HW	0.2177	0.8215	20.95	79.05	720.6	168.7	81.03	18.97
NRGO-HW	0.1718	0.6842	20.07	79.93	548.6	104.5	84.00	16.00
TRGO-JY	0.1945	0.7839	19.88	80.12	630.9	139.1	81.94	18.06
NRGO-JY	0.1826	0.7393	19.81	80.19	576.9	125.6	82.12	17.88

[a]Note: V_1, micropore volume, (0−2 nm); V_2, mesoporous pore volume, (2−36 nm); S_1, micropore specific surface area, (0−2 nm); S_2, mesoporous specific surface area, (2−36 nm); V_{Total}, total pore volume; S_{Total}, total specific surface area; $V_{x1} = V_1/(V_1 + V_2)$, $V_{x2} = V_2/(V_1 + V_2)$, $S_{x1} = S_1/(S_1 + S_2)$, and $S_{x2} = S_2/(S_1 + S_2)$.

Compared with T-HW/JY, the (I_{D1}/I_G) of N-HW/JY is larger and $(G−D_1)$ is smaller (Table 4), indicating that the order degree of TDC is relatively increased, which confirms that the occurrence of tectonic action will make the microcrystalline structure of coal relatively more orderly. After graphitization at 2800 °C, the D peak of each graphite is weak and almost disappears, the width of the G peak is reduced, and the peak becomes extremely sharp. At the same time, a strong G′ peak appears at ∼2700 cm⁻¹, which is very sensitive to the graphite layer accumulation along the c-axis, and the increase in aromatic fringe stacking (HRTEM) and interlayer accumulation N_{ave} parameter (XRD) mentioned

above explains this phenomenon well. Compared with each NG, the (I_{D1}/I_G) value of TG decreases, indicating that graphite prepared from TDC has a higher order degree than that from NSC. After oxidation treatment, the (I_{D1}/I_G) value increases; at the same time, the G′ peak representing the interlayer stacking mode disappears, indicating that the oxidant produces more lattice defects, heteroatoms, and functional groups, which reduces the order of GO. After thermal reduction to RGO, compared with TGO-HW, Figure 5b shows that D_1 and D_2 peaks in the D-peak band in TRGO-HW are significantly weaker, while the D_4 peak almost disappears, indicating that most of the sp²-type amorphous carbon,
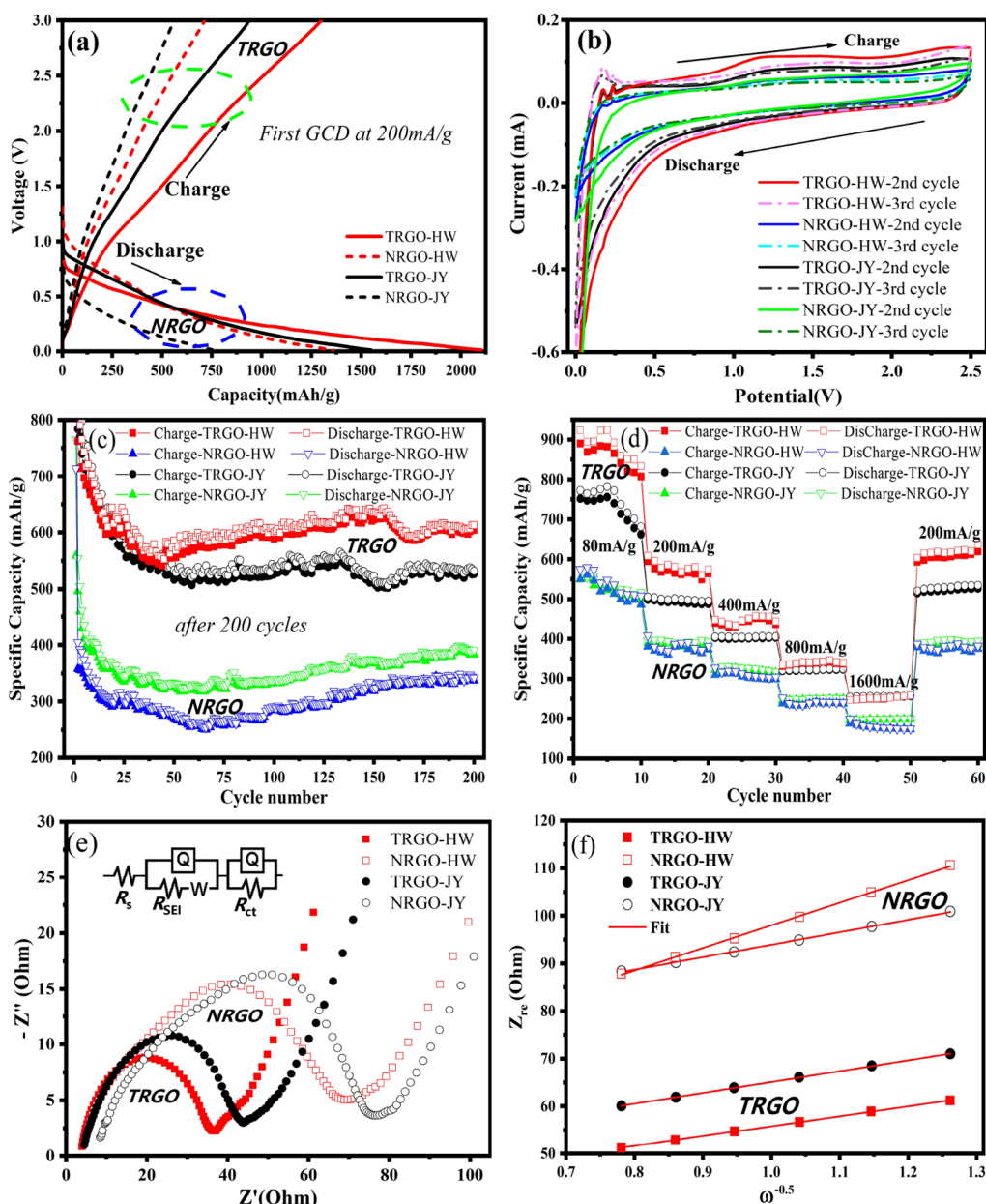
Figure 7. Electrochemical properties of TRGO/NRGO series products. (a) First GCD curves at 200 mAh/g; (b) second and third CV curves; (c) cycling stability of TRGO/NRGO after 200 cycles; (d) rate capability of TRGO/NRGO; (e) EIS behavior; (f) Warburg impedance coefficient fitting line.

oxygen-containing functional groups, and heterocyclic compounds on the surface of the sample slice are removed,[52] which increase the degree of RGO ordering. Comparing the (I_{D1}/I_G) and $(G-D_1)$ values of the two types of TRGO and NRGO, it can be seen that the TRGO crystal plane is closer to perfection, which is consistent with the HRTEM results.

3.4. Pore Structure Analysis. Figure 6a shows that the micropore (0.3–2 nm) pore volume distribution density function of the coal samples is mainly at pore diameters of 0.48 and 0.60 nm, showing a "double peak" fluctuation trend, and the growth rate of the specific surface area also reaches the maximum at this "double peak" (Figure 6d). Then, the density function of the pore volume distribution shows an overall attenuation trend with increasing pore diameter (Figure 6b,c), and the total pore specific surface area increased slowly (Figure 6e). The micropore volume (V_1) and specific surface area (S_1)

of coal account for more than 96% of its total pore volume (V_{Total}) and total specific surface area (S_{Total}), indicating that the micropores are absolutely dominant in the coal pore structure, and the difference of micropores is precisely caused by the different arrangement and combination of the molecular structure of coal.

Under the same geological conditions, the V_1, V_2, S_1, and S_2 of TDC are larger than those of NSC (Table 5), suggesting that the molecular structure of coal is activated under the influence of tectonic stress. On the one hand, polymerization forms the macromolecular structure of orientation growth,[24] which was previously confirmed by HRTEM, resulting in transformation of the pore system change from a closed system to an open system and the generation of new pores. On the other hand, the side chains and functional groups on the aromatic ring structure of coal will decompose to form low-

Table 6. Electrochemical Performance Parameters of Coal-Based Graphene Series Products[a]

sample numbers	first charge specific capacity (mAh/g)	first discharge specific capacity (mAh/g)	after 200 cycles reversible capacity (mAh/g)	after 200 cycles coulombic efficiency (%)	1600 mA·g^{-1} high-current reversible capacity (mAh/g)	return to 200 mA·g^{-1} reversible capacity (mAh/g)	charge transfer resistance (R_{ct}) (Ω)	Li$^+$ diffusion coefficient (D) (cm^2/s)
TRGO-HW	1301.4	2105.3	612.8	98.7	258.6	619.5	32.24	3.05×10^{-14}
NRGO-HW	713.9	1359.4	342.2	98.6	174.1	375.4	64.50	0.88×10^{-14}
TRGO-JY	939.1	1551.5	532.3	98.0	254.5	535.0	39.38	2.56×10^{-14}
NRGO-JY	557.2	765.3	391.3	98.9	197.2	395.0	68.04	1.93×10^{-14}

^{a}Note: $Z_{re} = R_{ct} + R_s + \sigma_w \omega^{-0.5}$; Z_{re}, the real part of the impedance; R_{ct}, charge-transfer resistance; R_s, SEI film resistance; σ_w the slope of the line made by $\omega^{-0.5}$, Z_{re}, Warburg impedance coefficient; ω, the angular frequency in the low-frequency region. $D = R^2 T^2/(2A^2 n^4 F^4 C^2 \sigma^2)$; D, the diffusion coefficient; R, molar gas constant (8.314 J mol^{-1} K^{-1}); T, the absolute temperature; A, the area of the electrode surface (cm^2); n, the number of electrons per molecule attending the electronic transfer reaction; F, Faraday's constant (96,500 C/mol); C, the molar concentration of Li$^+$; σ, Warburg impedance coefficient.

molecular-weight compounds and gaseous hydrocarbons,[27] promoting the weakening of the cross-linking system between coal molecular structures, dredging the pores and reducing the resistance to the growth of carbon sources in coal. This result shows that the tectonic stress has the functions of pore dredging, pore increasing, and pore enlarging in coal, which provide a relatively favorable growth space and driving force for the preparation of graphite from a carbon source in TDC.

Figure 6f−h shows the density function diagram of the pore volume distribution of each RGO. Compared with the "double-peak" distribution of its precursor coal, the density function diagram of RGO shows a "multipeak" distribution. The continuous appearance of new peaks indicates that the micropores and mesopores of each RGO significantly increased (Figure 6g−i). Table 5 shows that V_1, V_2, S_1, and S_2 of TRGO are significantly higher than those of NRGO. This occurs because the LMO domain vertical height (d) and the degree of graphitization (G) in the graphite microcrystalline structure prepared by TDC are better than those of NSC, resulting in that TG is easier to exfoliate RGO with rich graded porous nanochannels under the same conditions than NG, which confirmed that TDC is easier to prepare porous graphene products than NSC.

3.5. Electrochemical Performance Analysis. The prepared coal-based graphene series products was used as the anode material in LIBs, and its electrochemical lithium storage performance was tested and evaluated (Figure 7). Figure 7a shows the first GCD performance of TRGO-HW/JY and NRGO-HW/JY as anode materials at a current density of 200 mA/g. The first GCD specific capacity of TRGO-HW/JY is approximately twice that of NRGO-HW/JY (Table 6), which is higher than the theoretical capacity of 372 mAh/g of traditional graphite and better than the reversible specific capacity of 450 mAh/g of the coal-based graphene lithium battery prepared by Gao Shasha at the current density of 200 mA/g,[57] indicating that the electrochemical lithium storage performance of TRGO is obviously better. However, the first Coulombic efficiency of both TRGO and NRGO is low, indicating that the first GCD capacity of each RGO is largely lost, which is mainly due to the decomposition of the electrolyte on the electrode surface and the formation of the SEI film, resulting in the irreversible cycle of partial loss of the battery.[58] Then, the CV scanning curves of the second and third cycles have a high coincidence (Figure 7b), indicating that the structure of the SEI film and carbon material is

relatively stable and reversible. It is confirmed from the electrochemical performance that the electrochemical cycle stability of each coal-based graphene battery after the first GCD is good, which laid a good foundation for the extraction-insertion of lithium ions (Li$^+$) in the subsequent charging and discharging process.[59] After 200 cycles (Figure 7c), the reversible capacity of each material battery gradually stabilized, and the Coulombic efficiency reached more than 98.0%, indicating that after 200 cycles, the cycling stability and reversibility of the internal structure of each material battery were greatly enhanced. At this time, the reversible capacity of TRGO-HW/JY is 612.8/532.3 mAh/g, which is still much higher than the value of 342.2/391.3 mAh/g of NRGO-HW/JY. Therefore, compared with NRGO, the electrochemical performance of TRGO after cycle stabilization is also better. In addition, Figure 7d shows the rate capability of samples at different current densities (80, 200, 400, 800, 1600, and 200 mA/g). Although the reversible capacity of each sample continuously decreases with increasing current from 80 mA/g rises to 1600 mA/g, even under the high current density of 1600 mA/g, each TRGO retains a higher reversible capacity than NRGO. When it returns to a low current (200 mAh/g) again after a high rate cycle, the reversible capacity of TRGO-HW/JY recovers to 619.5/535 mAh/g, which is still higher than that of NRGO-HW/JY (375.4/395 mAh/g), indicating that the TRGO anode material has excellent rate capability and can meet the demand of high current charge and discharge.

To further study the dynamic diffusion of Li$^+$ in electrode materials, the diffusion coefficient (D) of Li$^+$ in the electrode was studied by electrochemical impedance technique.[60] Figure 7e shows the electrochemical impedance spectroscopy (EIS) of TRGO-HW/JY and NRGO-HW/JY after 200 cycles, and the diameter of the semicircle in the high- and medium-frequency regions can reflect the electrochemical impedance (conductivity) of Li$^+$ passing through the SEI film in the spectrum (Z' is the real part of the impedance and Z'' is the imaginary part of the impedance). The greater the resistance between the electrode and electrolyte, the larger the semicircle diameter. The low-frequency region is formed by a slope curve conforming to the semi-infinite diffusion model,[61,62] which is related to the Li$^+$ diffusion process and corresponds to the limited transfer Warburg impedance of Li$^+$ in the material.[63,64] The semicircle diameter of TRGO-HW/JY is smaller than that of NRGO-HW/JY (Figure 7e), so the charge-transfer resistance of TRGO is significantly lower than that of

NRGO (Table 6), indicating that Li$^+$ is more smoothly extracted in TRGO. As shown in Figure 7f, $\omega^{-0.5}$ has a linear relationship with Z_{re}, and the slope of the straight line obtained by fitting is the Warburg impedance coefficient (σ_w) of the electrode. According to the corresponding formula (Table 6), the diffusion coefficients (D) of TRGO-HW/JY are 3.05 × 10^{-14} and 2.56 × 10^{-14}, respectively, which are greater than those of NRGO/JY, 0.88 × 10^{-14} and 1.93 × 10^{-14}, reflecting the rapid diffusion speed of Li$^+$ in the TRGO battery.

Compared with NRGO, TRGO has an excellent large-size microcrystalline structure-oriented morphology, which can increase the storage space of Li$^+$ and reduce the crystal plane tortuosity of the material, thus reducing the surface charge-transfer resistance and resulting in an increase in the diffusion coefficient (D) of Li$^+$, which is conducive to the efficient conduction of Li$^+$. In addition, TRGO has more micropores, which can improve the Li$^+$-storage sites. The abundant mesopores can shorten the diffusion path of Li$^+$. A higher pore specific surface area can increase the contact area between the electrolyte and the electrode and provide more active sites for Li$^+$ migration. Compared with NRGO, TRGO has an excellent microcrystalline structure-oriented morphology and a relatively rich hierarchical porous volume and specific surface area structure. The synergistic effect of these two resulting in its high lithium storage capacity and low charge-transfer resistance leads to the rapid Li$^+$ diffusion rate of TRGO, making the TRGO material exhibit excellent lithium-storage performance, rate capability, and cycle stability.

4. CONCLUSIONS

TDC is often used as a low-value power coal due to its low mechanical strength, powdery shape, and difficulty in washing. However, long-term tectonic stress has improved the structure of the carbon source in coal. TDC with the short-range ordered microcrystalline orientation growth state indicates that there is more graphitizable carbon structures in the carbon source, which makes it easier to prepare TDC-based graphite with a perfect and ordered structure at the same temperature, resulting in TDC-based graphene not only having perfect and orderly crystal planes but also having rich nanochannels. High lithium-storage capacity and low charge-transfer resistance make the graphene made from TDC have better electrochemical performance as an anode material for LIBs, realizing the high additional-value utilization of TDC. The application research of stress in the preparation of high-performance carbon materials should be strengthened in the future. The main conclusions are as follows:

(1) Tectonic stress promotes the increase of the graphitizable carbon structure of carbon source in coal, which makes it easier to prepare perfect and orderly coal-based graphite by TDC than NSC. Tectonic stress makes the proportion of the medium-long aromatic fringes, the POD, and multilayer stacking of aromatic fringes in TDC slightly higher than those of NSC, while the relatively large microcrystalline size (L_a, L_c), short layer spacing (d_{002}), high order degree (I_{D1}/I_G), and more pore structures support the short-range ordered microcrystalline oriented growth state of the TDC carbon source. This indicates that tectonic stress promotes the increase of the graphitizable carbon structure of carbon source in coal and makes the vertical height (d) and degree of graphitization (G) of the graphite micro-

crystalline structure prepared by TDC better than those of NSC at the same temperature.

(2) Compared with NSC, the coal-based graphene prepared from TDC not only has more ordered and perfect crystal planes but also has rich nanochannels. The proportions of medium-long aromatic fringes, POD, and multilayer stacking in the aromatic fringes of TDC-based graphene (TRGO) are better than those of NSC-based graphene (NRGO). The larger microcrystalline sizes L_a, L_c and the smaller d_{002} and I_{D1}/I_G values show that the TRGO crystal plane is more perfect and orderly. The pore volume and specific surface area of microporous (0−2 nm) and mesoporous (2−38 nm) TRGO are much larger than those of NRGO.

(3) Compared with the NRGO battery, the diffusion speed of Li$^+$ in the TRGO battery is rapid. TRGO has an excellent microcrystalline structure-oriented morphology, relatively rich hierarchical porous volume, and specific surface area structure. The synergistic effect of these two resulting in its high lithium-storage capacity and low charge-transfer resistance leads to the rapid Li$^+$ diffusion rate of TRGO.

(4) TRGO has better electrochemical performance as an anode material for LIBs. The first GCD specific capacity of TRGO is approximately twice that of NRGO. After 200 cycles, the reversible capacity of the two sets of TRGO-HW/JY batteries is 612.8/532.3 mAh/g, which is still much higher than that of NRGO-HW/JY (342.2/391.3 mAh/g). When it returns to a low current again after a high rate cycle, the reversible capacity of TRGO is still higher than that of NRGO. The results show that the TRGO anode material has excellent lithium-storage performance, cycle stability, and rate capability.

■ ASSOCIATED CONTENT

Data Availability Statement

All relevant data are within the paper.

■ AUTHOR INFORMATION

Corresponding Author

Yugui Zhang − *School of Safety Science and Engineering, Henan Polytechnic University, Jiaozuo 454003, P.R. China; State Key Laboratory Cultivation Base for Gas Geology and Gas Control of Henan Province, Jiaozuo 454003, P.R. China;* Email: zyg@hpu.edu.cn

Authors

Hang Zhang − *School of Safety Science and Engineering, Henan Polytechnic University, Jiaozuo 454003, P.R. China;* orcid.org/0000-0003-2568-8828

Jian Li − *School of Safety Science and Engineering, Henan Polytechnic University, Jiaozuo 454003, P.R. China;* orcid.org/0000-0002-8117-9449

Zhangnan Ma − *School of Chemistry and Chemical Engineering, Henan Polytechnic University, Jiaozuo 454003, P.R. China*

Complete contact information is available at:
https://pubs.acs.org/10.1021/acsomega.3c02073

Author Contributions

H.Z.: data curation, experimental design, test, formal analysis, and writing-original draft. Y.Z.: conceptualization, funding

acquisition, and supervision. L.J.: data curation, test, and formal analysis. Z.M.: data curation and test.

Notes

The authors declare no competing financial interest.

The work is original and has not been published previously or is not under consideration for publication elsewhere. If accepted, it will not be published elsewhere in any form without a copyright holder.

■ ACKNOWLEDGMENTS

■ NOMENCLATURE

TDC	tectonically deformed coal
NSC	normal structural coal
HW	Hongwei Mine, Leiyang city, Hunan Province, China
JY	Jiyuan Mine, Jiyuan city, Henan Province, China
TG	graphite prepared from tectonically deformed coal
NG	graphite prepared from normal structural coal
GO	graphene oxide
RGO	graphene (reduced graphene oxide)
TRGO	graphene prepared from tectonically deformed coal
NRGO	graphene prepared from tectonically deformed coal
T-HW	sample number of tectonically deformed coal of Hongwei after deashing
N-HW	sample number of normal structural coal of Hongwei after deashing
T-JY	sample number of tectonically deformed coal of Jiyuan after deashing
N-JY	sample number of normal structural coal of Jiyuan after deashing
POD	preferred orientation degree
LMO	local molecular-oriented
L_a	crystallite width
L_c	crystallite height
d_{002}	interlayer spacing
N_{ave}	average number of aromatic layers
G	graphitization degree
GCD	galvanostatic charge−discharge
EIS	electrochemical impedance spectroscopy

■ REFERENCES

(1) Buseck, P. R.; Beyssac, O. From Organic Matter to Graphite: Graphitization. *Elements* **2014**, *10*, 421−426.

(2) Singh, V.; Joung, D.; Zhai, L.; Das, S.; Khondaker, S. I.; Seal, S. Graphene based materials: Past, present and future. *Prog. Mater. Sci.* **2011**, *56*, 1178−1271.

(3) Franklin, R. E. The structure of graphitic carbons. *Acta Crystallogr.* **1951**, *4*, 253−261.

(4) Franklin, R. E. Crystallite Growth in Graphitizing and Non-Graphitizing Carbons. *Proc. R. Soc. London, Ser. A* **1951**, *209*, 196−218.

(5) Rouzaud, J. N.; Oberlin, A. Structure, microtexture, and optical properties of anthracene and saccharose-based carbons. *Carbon* **1989**, *27*, 517−529.

(6) Wang, G. F. Carbonaceous material in the Ryoke metamorphic rocks, Kinki district, Japan. *Lithos* **1989**, *22*, 305−316.

(7) Landis, C. A. Graphitization of dispersed carbonaceous material in metamorphic rocks. *Contrib. Mineral. Petrol.* **1971**, *30*, 34−45.

(8) Diessel, C. F. K.; Brothers, R. N.; Black, P. M. Coalification and graphitization in high-pressure schists in New Caledonia. *Contrib. Mineral. Petrol.* **1978**, *68*, 63−78.

(9) Bonijoly, M.; Oberlin, M.; Oberlin, A. A possible mechanism for natural graphite formation. *Int. J. Coal Geol.* **1982**, *1*, 283−312.

(10) Wada, H.; Tomita, T.; Matsuura, K.; Tuchi, K.; Ito, M.; Morikiyo, T. Graphitization of carbonaceous matter during metamorphism with references to carbonate and pelitic rocks of contact and regional metamorphisms. *Contrib. Mineral. Petrol.* **1994**, *118*, 217−228.

(11) Suchy, V.; Frey, M.; Wolf, M. Vitrinite reflectance and shear-induced graphitization in orogenic belts: A case study from the Kandersteg area. *Int. J. Coal Geol.* **1997**, *34*, 1−20.

(12) Ghazinejad, M.; Holmberg, S.; Pilloni, O.; Oropeza-Ramos, L.; Madou, M. Graphitizing Non-graphitizable Carbons by Stress-induced Routes. *Sci. Rep.* **2017**, *7*, 16551.

(13) Bustin, R. M.; Rouzaud, J. N.; Ross, J. V. Natural graphitization of anthracite: Experimental considerations. *Carbon* **1995**, *33*, 679−691.

(14) De Fonton, S.; Oberlin, A.; Inagaki, M. Characterization by electron microscopy of carbon phases (intermediate turbostratic phase and graphite) in hard carbons when heat-treated under pressure. *J. Mater. Sci.* **1980**, *15*, 909−917.

(15) Beyssac, O.; Rouzaud, J.; Goffé, B.; Brunet, F.; Chopin, C. Graphitization in a high-pressure, low-temperature metamorphic gradient: a Raman microspectroscopy and HRTEM study. *Contrib. Mineral. Petrol.* **2002**, *143*.

(16) Yan, Y.; Gao, W.; Yang, Z.; Zhang, L.; Ran, J. Preparation of coal-based graphene and application research advances of graphene in the field of thermal conduction. *J. China Coal Soc.* **2020**, *45*, 443−454.

(17) Rodrigues, S.; Suárez-Ruiz, I.; Marques, M.; Flores, D.; Camean, I.; García, A. B. Development of graphite-like particles from the high temperature treatment of carbonized anthracites. *Int. J. Coal Geol.* **2011**, *85*, 219−226.

(18) Huan, X.; Tang, Y.; Xu, J.; Lan, C.; Wang, S. Structural characterization of graphenic material prepared from anthracites of different characteristics: A comparative analysis. *Fuel Process. Technol.* **2019**, *183*, 8−18.

(19) Powell, C.; Beall, G. W. Graphene oxide and graphene from low grade coal: Synthesis, characterization and applications. *Curr. Opin. Colloid Interface Sci.* **2015**, *20*, 362−366.

(20) Wang, L.; Zhang, H.; Li, Y. On the difference of characterization and supercapacitive performance of graphene nanosheets from precursors of inertinite- and vitrinite-rich coal. *J. Alloys Compd.* **2020**, *815*, No. 152502.

(21) Xing, B.; Zeng, H.; Guo, H.; Xu, B.; Kang, W.; Zhang, C.; Huang, G.; Sun, Q.; Zhang, B. Preparation of coal-based graphite nanoplatelets based on mechanochemistry and the characterization of their electrochemical energy storage performance. *J. China Coal Soc.* **2022**, *47*, 958−968.

(22) Zhang, Y.; Zhang, K.; Jia, K.; Liu, G.; Ren, S.; Li, K.; Long, X.; Li, M.; Qiu, J. Preparation of coal-based graphene quantum dots/α-Fe2O3 nanocomposites and their lithium-ion storage properties. *Fuel* **2019**, *241*, 646−652.

(23) Yu, S.; Bo, J.; Vandeginste, V.; Mathews, J. P. Deformation-related coalification: Significance for deformation within shallow crust. *Int. J. Coal Geol.* **2022**, *256*.

(24) Zhang, X.; Wang, W.; Zhang, Y.; Gao, F.; Huan, X. Oriented growth mechanism of tectonic coal microcrystal. *J. China Coal Soc.* **2016**, *41*, 712−718.

(25) Cao, Y.; Davis, A.; Liu, R.; Liu, X.; Zhang, Y. The influence of tectonic deformation on some geochemical properties of coals—a possible indicator of outburst potential. *Int. J. Coal Geol.* **2003**, *53*, 69−79.

(26) Cao, Y. X. Deformed-coal structure and control to coal-gas outburst. *J. China Coal Soc.* **2007**, *3*, 281−284.

(27) Cao, D.; Li, X.; Zhang, S. Effect of tectonic stress on coalification—Stress degradation mechanism and stress polycondensation mechanism. *Sci. China (Earth Sci.)* **2006**, *36*, 59−68.

(28) Zhang, Y.; Zhang, Z.; Xie, K. Mechanochemistry and Structure of Tectonic Coal During Coal Evolution. *J. Henan Polytech. Univ.* **2005**, *24*, 95−99.

(29) Bonaccorso, F.; Colombo, L.; Yu, G.; Stoller, M.; Tozzini, V.; Ferrari, A. C.; Ruoff, R. S.; Pellegrini, V. Graphene, related two-dimensional crystals, and hybrid systems for energy conversion and storage. *Science* **2015**, *347*, 41−41.

(30) Qian, W.; Fu, H.; Sun, Y.; et al. Scalable Assembly of High Quality Graphene Films Via Electrostatic Repulsion Aligning. *Adv. Mater.* **2022**, *34*, No. e2206101.

(31) Wang, Z.; Mao, B.; Zhao, M.; et al. Ultrafast Macroscopic Assembly of High-Strength Graphene Oxide Membranes by Implanting an Interlaminar Superhydrophilic Aisle. *ACS Nano* **2022**, 3934.

(32) Ju, Y.; Jiang, B.; Hou, Q.; Wang, G. The new structure-genetic classification system in tectonically deformed coals and its geological significance. *J. China Coal Soc.* **2004**, *29*, 513−517.

(33) Wang, E.; Liu, M.; Wei, J. New genetic-texture-structure classification system of tectonic coal. *J. China Coal Soc.* **2009**, *34*, 656−660.

(34) Nyathi, M.; Clifford, C.; Schobert, H. Characterization of graphitic materials prepared from different rank Pennsylvania anthracites. *Fuel* **2013**, *114*, 244.

(35) Botas, C.; Pérez-Mas, A. M.; Álvarez, P.; Santamaría, R.; Menéndez, R. Optimization of the size and yield of graphene oxide sheets in the exfoliation step. *Carbon* **2013**, *63*, 576−578.

(36) Botas, C.; Álvarez, P.; Blanco, P.; Granda, M.; Menéndez, R. Graphene materials with different structures prepared from the same graphite by the Hummers and Brodie methods. *Carbon* **2013**, *65*, 156−164.

(37) Mathews, J. P.; Sharma, A. The structural alignment of coal and the analogous case of Argonne Upper Freeport coal. *Fuel* **2012**, *95*, 19−24.

(38) Louw, E. Structure and combustion reactivity of inertinite-rich and vitrinite-rich South African coal chars: Quantification of the structural factors contributing to reactivity differences. PhD thesis, The Pennsylvania State University, USA, 2012.

(39) Sonibare, O. O.; Haeger, T.; Foley, S. F. Structural characterization of Nigerian coals by X-ray diffraction, Raman and FTIR spectroscopy. *Energy* **2010**, *35*, 5347−5353.

(40) Sheng, C. Char structure characterised by Raman spectroscopy and its correlations with combustion reactivity. *Fuel* **2007**, *86*, 2316−2324.

(41) Langmuir, I. The adsorption of gases on plane surfaces of glass, mica and platinum. *J. Am. Chem. Soc.* **1918**, *40*, 1361−1403.

(42) Thommes, M. Physisorption of gases, with special reference to the evaluation of surface area and pore size distribution (IUPAC Technical Report). *Pure Appl. Chem.* **2016**, *87*, 1051−1069.

(43) Li, Y.; Zhang, Y.; Zhang, L.; Hou, J. Characterization on pore structure of tectonic coals based on the method of mercury intrusion, carbon dioxide adsorption and nitrogen adsorption. *J. China Coal Soc.* **2019**, *44*, 1181−1196.

(44) Zhang, Z.; Yang, Z. Theoretical and practical discussion of measurement accuracy for physisorption with micro- and mesoporous materials. *Chin. J. Catal.* **2013**, *34*, 1797−1810.

(45) Sharma, A.; Kyotani, T.; Tomita, A. Direct Observation of Raw Coals in Lattice Fringe Mode Using High-Resolution Transmission Electron Microscopy. *Energy Fuels* **2000**, *14*, 1219−1225.

(46) Song, Y.; Jiang, B.; Li, M.; Hou, C.; Mathews, J. P. Macromolecular transformations for tectonically-deformed high volatile bituminous via HRTEM and XRD analyses. *Fuel* **2020**, *263*, No. 116756.

(47) Mathews, J. P.; Fernandez-Also, V.; Jones, A. D.; Schobert, H. H. Determining the molecular weight distribution of Pocahontas No.3 low-volatile bituminous coal utilizing HRTEM and laser desorption ionization mass spectra data. *Fuel* **2010**, *89*, 1461−1469.

(48) Zheng, Z.; Zhang, J.; Huang, J. Y. Observations of microstructure and reflectivity of coal graphites for two locations in China. *Int. J. Coal Geol.* **1996**, *30*, 277−284.

(49) Kwiecińska, B.; Petersen, H. I. Graphite, semi-graphite, natural coke, and natural char classification—ICCP system. *Int. J. Coal Geol.* **2004**, *57*, 99−116.

(50) Zhang, H.; Zhang, Y.; Lei, D.; Jiao, Y. Characterization of structure of kaolinite in tectonically deformed coal: evidence of mechanochemistry. *Energy Sources, Part A* **2021**, *5*, 1−12.

(51) Li, J.; Qin, Y.; Chen, Y.; Song, Y.; Wang, Z. HRTEM observation of morphological and structural evolution of aromatic fringes during the transition from coal to graphite. *Carbon* **2022**, *187*, 133−144.

(52) Tang, Y.; Xu, J.; Huan, X.; Wang, S.; Chen, P. Preparation and spectroscopic characterization of coal-based graphene from anthracite in Xiaofalu, Yunnan, China. *J. China Coal Soc.* **2020**, *45*, 740−748.

(53) Zhou, Q.; Zhao, Z.; Zhang, Y.; Meng, B.; Zhou, A.; Qiu, J. Graphene Sheets from Graphitized Anthracite Coal: Preparation, Decoration, and Application. *Energy Fuel* **2012**, *26*, 5186−5192.

(54) Baysal, M.; Yürüm, A.; Yıldız, B.; Yürüm, Y. Structure of some western Anatolia coals investigated by FTIR, Raman, 13C solid state NMR spectroscopy and X-ray diffraction. *Int. J. Coal Geol.* **2016**, *163*, 166−176.

(55) Vijapur, S. H.; Wang, D.; Ingram, D. C.; Botte, G. G. An investigation of growth mechanism of coal derived graphene films. *Mater. Today Commun.* **2017**, *11*, 147−155.

(56) Sadezky, A.; Muckenhuber, H.; Grothe, H.; Niessner, R.; Pöschl, U. Raman microspectroscopy of soot and related carbonaceous materials: Spectral analysis and structural information. *Carbon* **2005**, *43*, 1731−1742.

(57) Gao, S. Preparation and electrochemical performance of coal-based porous carbon and molybdenum-based composites. PhD thesis, The Xinjiang University, China, 2019.

(58) Zhang, Y.; Li, K.; Ren, S.; Zhang, Y.; Liu, G.; Zhou, A. Coal-based graphene/Fe2O3 nanostructures grow on nickel foams as an enhanced free-standing anode for lithium-ion batteries. *J. China Coal Soc.* **2021**, *46*, 1173−1181.

(59) Zheng, C.; Hu, X.; Sun, X.; Yoo, S. J.; Li, X. Large-scale synthesis of nitrogen-rich hierarchically porous carbon as anode for lithium-ion batteries with high capacity and rate capability. *Electrochim. Acta* **2019**, *306*, 339−349.

(60) Zhe, L.; Fei, D.; Bie, X.; Dong, Z.; Wei, Y. Electrochemical kinetics of the Li $[Li_{0.23}Co_{0.3}Mn_{0.47}]$ O$_2$ cathode material studied by GITT and EIS. *J. Phys. Chem. C* **2010**, *114*, 22751−22757.

(61) Shaju, K. M.; Rao, G. V. S.; Chowdari, B. V. R. Electrochemical Kinetic Studies of Li-Ion in O$_2$-Structured Li$_{2/3}$ (Ni1/3Mn2/3) O2 and Li (2/3) + x (Ni1/3Mn2/3) O2 by EIS and GITT. *J. Electrochem. Soc.* **2002**, *150*, A1−A13.

(62) Ali, G.; Patil, S.; Mehboob, S.; et al. Determination of lithium diffusion coefficient and reaction mechanism into ultra-small nanocrystalline SnO$_2$ particles. *J. Power Sources* **2019**, *419*, 229−236.

(63) Choi, B. G.; Chang, S. J.; Lee, Y. B.; Bae, J. S.; Kim, H. J.; Huh, Y. S. 3D heterostructured architectures of Co3O4 nanoparticles deposited on porous graphene surfaces for high performance of lithium ion batteries. *Nanoscale* **2012**, *4*, 5924−5930.

(64) Chen, S.; Bao, P.; Huang, X.; Sun, B.; Wang, G. Hierarchical 3D mesoporous silicon@graphene nanoarchitectures for lithium ion batteries with superior performance. *Nano Res.* **2014**, *7*, 85−94.